

3D NUMERICAL MODELS FOR ALONG-AXIS VARIATIONS IN DIKING AT
MID-OCEAN RIDGES

by

Xiaochuan Tian

A Thesis

Submitted in Partial Fulfillment of the
Requirements for the Degree of
Master of Science

Major: Geophysics

The University of Memphis

May, 2015

Copyright © 2015 Xiaochuan Tian

All rights reserved

Dedication

I would like to dedicate this Thesis to my mother, Xia Tian, the most important person in my life. Without her guidance and support, I will not become who I am.

Acknowledgements

To Eunseo,
To Committee members,
To CERI,

Abstract

Tian, Xiaochuan. M.S. The University of Memphis. May 2015. 3D Numerical Models for Along-axis Variations in Diking at Mid-Ocean Ridges. Major Professor: Eunseo Choi.

Bathymetry of ocean floors reveals a great variety of morphologies at Mid-ocean Ridges (MORs). Previous studies showed that the morphologies at slow spreading MORs are mainly controlled by the ratio between rates of magma supply and plate extension. 2D models for the across-ridge cross-sections have been successful in explaining many of the observed morphological features such as abyssal hills and oceanic core complexes. However, the magma supply varies along the ridge and the interaction between the tectonic plates and magmatism at MORs are inevitably 3D processes. We propose to investigate the consequences of the along-axis variability in diking in terms of faulting pattern and the associated structures. This work will include implementation of an algorithm of parameterizing repeated diking in a 3D parallel geodynamic modeling code.

Table of Contents

Chapter	Page
1 Introduction	1
1.1 Research Questions	1
1.2 Review of Literature	1
1.3 Statement of Research Purpose	5
1.4 Findings	6
2 Methods	7
2.1 Method of approach	7
2.2 Model Setup	9
2.3 Parameters to control	9
3 3D Results	11
3.1 Reference models	12
3.1.1 M varies along the ridge-axis	12
3.1.2 Constant M along the ridge-axis	18
3.2 Tables of all the data points	19
3.3 Variation of the functional form	21
3.3.1 Comparing M ₂₈ in terms of linear, sinusoidal and square root	21
3.4 Variation of the range of M	25
3.5 Influence of weakening rate	25
3.6 Fault Alternation	25
3.7 Corrugation	25
3.8 Summary of Findings	25
4 Discussion	27
4.1 Discussion of Findings	27

4.2	Fault alternation	27
4.2.1	Alternating on conjugate plate	27
4.2.2	Secondary near-axis normal fault	27
4.3	Influence of healing	28
4.4	Comparing model results with nature observation	28
4.5	Parallel computing efficiency	28
4.6	Model Limitation	28
4.7	Reccommendation for Future Research	28
5	Conclusions	29

1 Introduction

Around 70% of the Earth's crust is oceanic crust and the mid-ocean ridges (MORs), the longest mountain chains on the Earth, are where new crust are forming with a multitude of seismic and volcanic activities. To study how new crust is created and how MORs evolve is significant for Earth Sciences. Geodynamic modeling along with a variety of geological, geophysical observation and lab experiment constraints have been used to study how the MORs work as a system under geological time scale.

1.1 Research Questions

High-resolution multi-beam bathymetry has revealed various characteristics of topography along and across MOR axis. Three specific questions stimulate people's interests most. First, what causes the distinct difference in axial topography between slow and fast spreading ridges. Second, for slow spreading ridges, why does topography along ridge varies and how to explain many features observed. Third, why do oceanic core complexes (OCCs) form and what is the mechanism.

1.2 Review of Literature

According to [Fowler, 2004], variations in mid-ocean ridge morphologies are mainly controlled by four factors: magma supply, tectonic strain, hydrothermal circulation and spreading rate. Among them, the spreading rate is the most important. Slow-to-intermediate spreading centers (half spreading rate less than 4cm/year) produce median valleys that are typically 10~20km wide and 1~2km deep (e.g., Mid-Atlantic Ridges, Figure 1(a)). Fast-spreading centers (half spreading rate greater than 5cm/year) have axial highs that are 10~20 km wide, 0.3~0.5 km high (e.g., East Pacific Rise, Figure 1(b)).

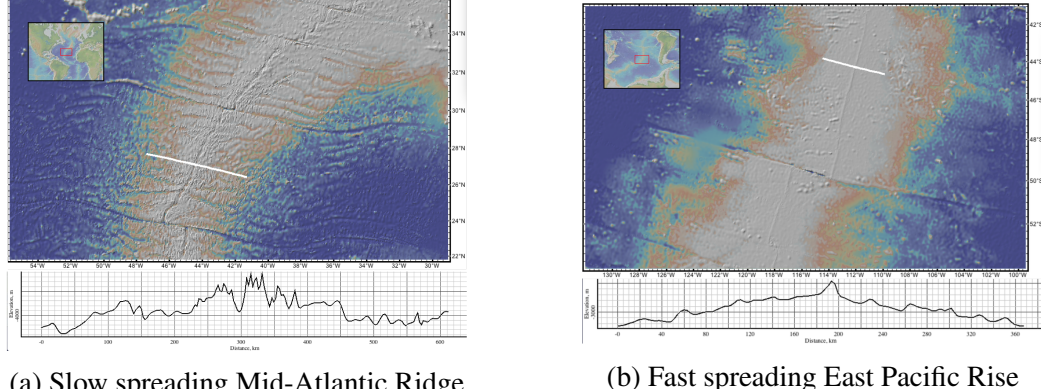


Figure 1: Profiles of bathymetry across MORs.

Slow spreading ridges exhibit along-axis variations as well in terms of the width and depth of median valleys and the off-axis morphology. Figure 2 shows that the topographic profile nearer to the center of the ridge segment (A-A') is rather symmetric and has higher frequency. The maximum relief is about 1km. In contrast, the near-tip profile (B-B') is asymmetric and has much lower frequency and a greater relief (~ 3 km). The bathymetry and crustal thickness along the ridge valley also varies. From [Chen and Lin, 1999], the maximum along-axis variation in crustal thickness ΔH_c is linearly increasing with segment length L , and the relationship is $\Delta H_c(L) = 0.0206L$ (Figure 3).

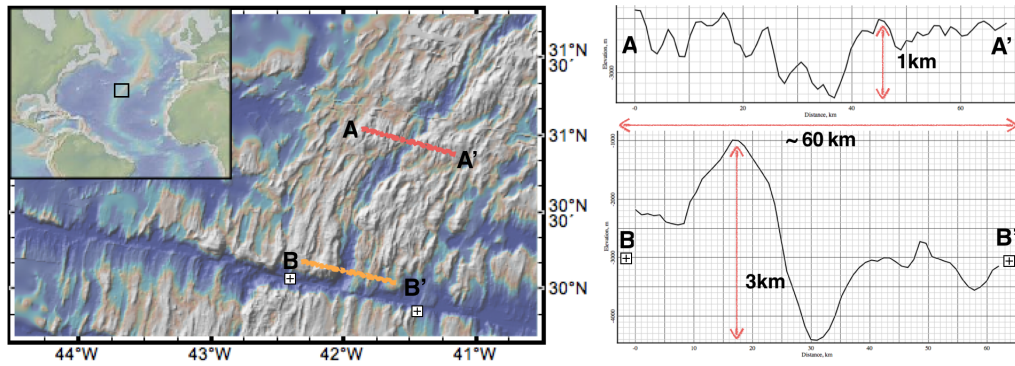


Figure 2: Two bathymetry cross-sections of Mid-Atlantic Ridge (MAR) with 10 times vertical exaggeration. A-A' is closer to the ridge segment center while B-B' is at the tip of the segment near the Atlantis Transform fault.

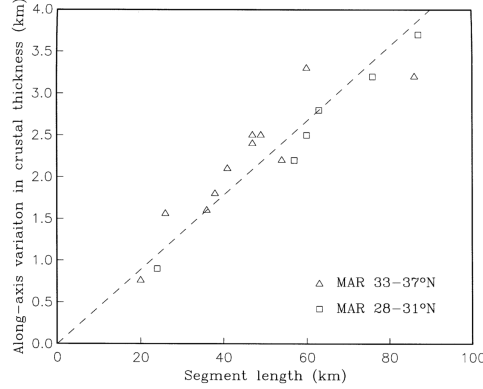


Figure 3: Relationship between the maximum crustal thickness variations along a ridge segment and the segment length. The dashed line is the best-fit linear regression of the combined data. [Chen and Lin, 1999]

Magma supply at MORs is mostly a passive process when no hot plume presents [Fowler, 2004]. Hot mantle rises up to fill the vacated room being created by plate separation and decompression will lead to partial melting of the hot mantle. The melt upwells due to both pressure difference and buoyancy from lateral density difference. When the melt solidifies near the surface, it forms new crust. This diking process can also release extensional stresses result from far-field driving forces.

The passive nature of magma supply results in the major difference between fast and slow spreading ridges in the amount of magma supply. At the fast spreading ridges, magma supply is always sufficient for accommodating plate separation by filling the space by dikes. However, the amount of magma supplied in the form of dikes is not as much at slow spreading ridges and the oceanic lithosphere experiences internal deformations (i.e. tectonics process like normal faulting) when the accumulated extensional stress exceeds the strength of the crust.

Buck et al. [2005] attributed the contrasting faulting patterns and ocean floor morphology of fast- and slow-spreading ridges to the difference in the amount of plate extension accommodated by diking. They defined the ratio between the rates of diking and plate separation as $M = V_{dx}/2V_x$, where V_{dx} is the extensional velocity of a widening dike and V_x is the half spreading rate of the MOR. According to this definition, $M = 1$ represents the case

where diking is frequent enough to release all the tensional stresses from plate separation. $M = 0$ corresponds to the case of no magma supply, in which diking does not account for any of the plate motion and therefore plates kinematics requires plates to go through internal deformations. As shown in Figure 4, an axial high forms at a fast spreading ridge ($M=1$) due to buoyancy from lateral density difference across ridge axis but a median valley forms at a slow-spreading ridge ($M=0.5$) due to near-axis normal faulting, which is in turn caused by the stretching of oceanic lithosphere.

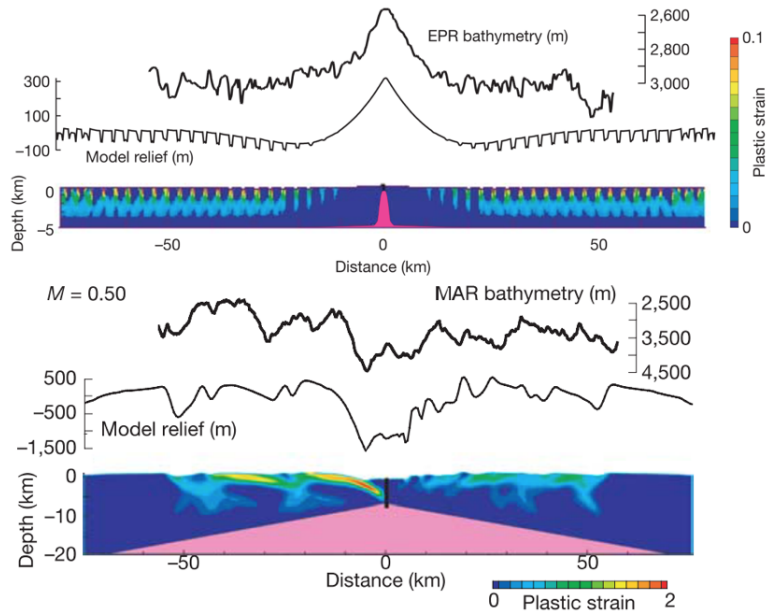


Figure 4: Upper one: modeling result for fast spreading agrees well with the observation of East Pacific Rise. Lower one: modeling result for slow spreading ridges agrees well with the bathymetry of Mid Atlantic Ridge. [Buck et al., 2005]

Tucholke et al. [2008] expanded the investigation on the role of M in the mid-ocean ridge mechanics. They focused on faulting behaviors of slow spreading ridges and find that the OCCs are most likely to form when M varies from 0.3 to 0.5. As shown in Figure 5, when $M=0.7$, repeated diking pushes faults forming at the spreading center away from axis. Since the thickness of the brittle layer increases away from the ridge axis, frictional and bending energy for maintaining the fault also increases. When it exceeds the energy for breaking a new near-axis fault, the old fault will be replaced by the new one. When

$M=0.3\sim0.5$, the normal faults remains active for a long time to become detachment faults, exhuming the lower crust and mantle materials to the seafloor. When M is less than 0.3, most of the tension is accommodated by intra-plate deformations rather than by diking and as a result, faulting pattern is more complicated and unsteady.

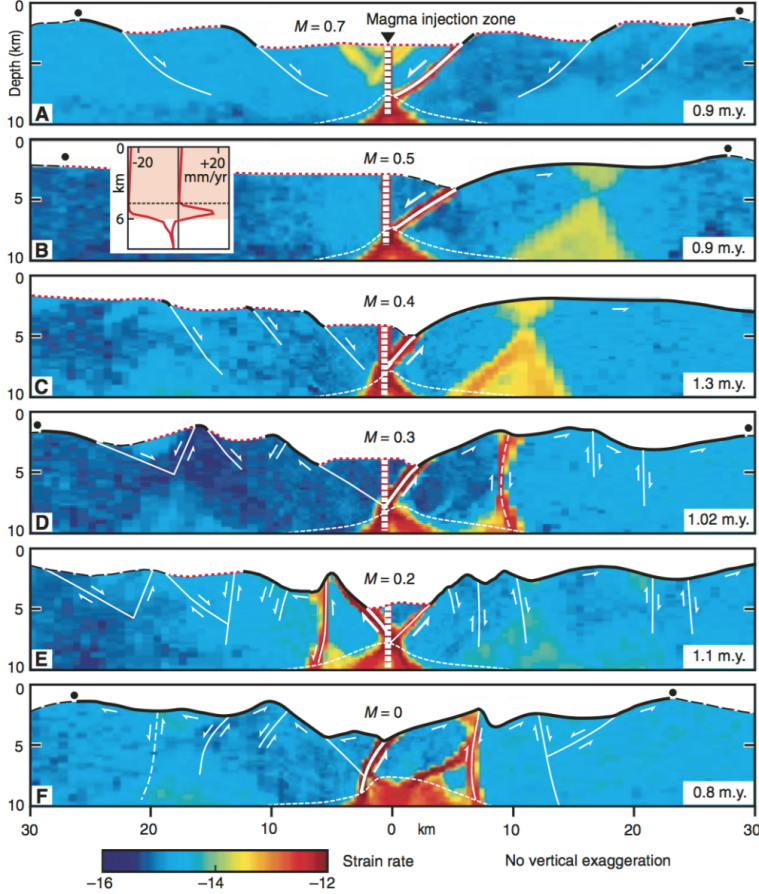


Figure 5: A~F: Faulting behavior for different values of M . Geologic interpretation is superimposed on modeled distribution of strain rate. Dots show breakaways of initial faults. Dashed seafloor is original model seafloor, red dotted seafloor is formed dominantly by magmatic accretion, and solid bold is fault surface. Note that detachment faults in B and C are not interrupted by secondary faults. [Tucholke et al., 2008]

1.3 Statement of Research Purpose

The M -factor formulation used in these previous 2D models successfully explained major features found in across-ridge profiles of seafloor bathymetry. However, 2D models have limitations in studying the along ridge-axis interactions, especially when important variables are not constant along the ridge axis. Magma supply at fast spreading ridges seems always sufficient for accommodating plate motions with little variation along the ridge axis. The relatively uniform topography along fast spreading ridges is considered to be consis-

tent with the uniformly abundance of magma supply. However, along the slow spreading ridges, bathymetry, gravity anomaly and results from reflection and refraction seismology show good correlation with variation in crustal thickness [Ryan et al., 2009, Chen and Lin, 1999, Lin et al., 1990, Tolstoy et al., 1993]. Because oceanic crust is mainly formed by upwelled magma at the ridge, variation in the thickness of the crust implies variation in magma supply. At slow spreading ridges, hydrothermal cooling, thermal structures and even local spreading rate [Baines et al., 2008] also varies both along and across the ridge axis and they appear interrelated. Thus, for slow-to-intermediate spreading ridges, the interactions between tectonics and magmatism at MORs are inevitably 3D processes and 3D numerical models are desirable for better understanding factors controlling both across-and along-ridge variations.

1.4 Findings

2 Methods

The purpose of this thesis is to study how the along-ridge variation in M will make a contribution to the observed various topography assuming that M is the first order control over the topography evolution of MORs governing the interaction between magmatism and tectonic deformations. We will extend the M-factor formulation originally developed for 2D models to 3D by implementing it into a 3D numerical modeling code SNAC [Choi et al., 2008]. We will focus on studying the last two questions mentioned in the introduction: 1) why does topography along ridge varies and how to explain many features observed; 2) why do OCCs form and what is the mechanism.

By systematically exploring the behaviors of the 3D models and comparing them with observations, we will be able to better understand how the mid-ocean ridge magmatism and tectonic deformations interact.

2.1 Method of approach

The numerical modeling code, SNAC, is an explicit Lagrangian finite element code. It solves the force balance equation for elasto-visco-plastic materials. Figure 6 shows major parts of the SNAC's algorithm.

For each time step dt , strain and strain rates are updated based on the boundary conditions shown in Figure 7. A constitutive model returns updated stresses corresponding to these deformation measures. Internal forces are then calculated from the update stresses, which is plugged into the momentum balance equation together with the body force term. Then, the net force divided by internal mass yields acceleration at a node point, which is time-integrated to velocity and displacement.

A 3D domain is discretized into hexahedral elements, each of which is in turn divided into two sets of tetrahedra. This symmetric discretization prevents faulting from favoring a specific direction or “mesh grains”.

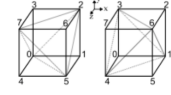
Rheology for the oceanic lithosphere is assumed to be elasto-visco-plastic. When viscosity is high at low temperature, the rheology essentially becomes the Mohr-Coulomb plasticity with strain softening and thus can create shear bands that behave like faults. Strain softening is realized by cohesion decreasing with increasing amount of permanent (i.e., plastic) strain. We assume this relationship is linear for simplicity such that it is sufficient for a full description of strain weakening to define initial and final values of cohesion and a critical plastic strain at which cohesion becomes the final value. We define the rate of strain weakening as the cohesion difference divided by the critical plastic strain and use it as one of the model parameters. When temperature is high and viscosity is low, the rheology becomes the Maxwell viscoelasticity and can model creeping flow. By assuming an appropriate initial temperature distribution, we can effectively set up a structure of a brittle lithosphere and a ductile asthenosphere. Rheological parameters are taken from previous studies that used a similar rheology [Buck 2005; Tuckholke et al., 2008] or from lab experiments [e.g., Kirby and Kronenberg, 1987].

For 3D diking processss, the expanding strain $\Delta\varepsilon_{xx}$ results from diking at the ridge will lead to extra-stresses in all three directions $\Delta\sigma_{xx}$, $\Delta\sigma_{yy}$ and $\Delta\sigma_{zz}$ based on the constitutive equations $\sigma_{ij} = \delta_{ij}\lambda\varepsilon_{ij} + 2\mu\varepsilon_{ij}$.

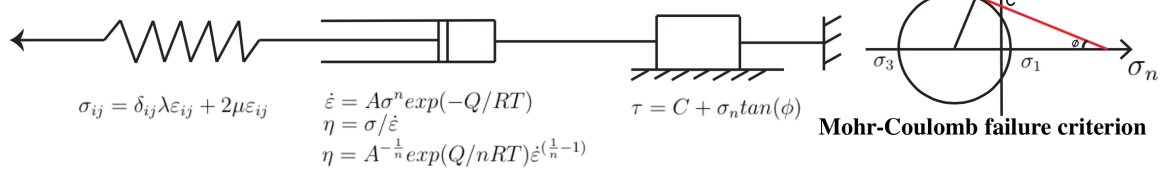
SNAC: a 3D, MPI parallelized, updated Lagrangian explicit finite difference code for modeling long-term tec-tonic evolution of the Earth's elasto-visco-plastic crust and mantle. (Choi et al., 2008)

Momentum Balance Equation: $\frac{\partial\sigma_{ij}}{\partial x_j} + \rho g_i = \rho \frac{Dv_i}{Dt}$

Spatial Decritization: A 3D domain is discretized into hexahedral elements, each of which is filled with two sets of 5 tetrahedra.



Elasto-Visco-Plastic (EVP) Rheology:



Diking M Formulation: $\text{M= } Vdx / 2Vx$ (Vdx is the dike accretion strain(dike widening) $\Delta\varepsilon_{xx}$ in each time step dt)

Stresses introduced by a dike accretion strain(dike widening) $\Delta\varepsilon_{xx}$ in each time step dt:

$$\Delta\sigma_{xx} = (\lambda + 2\mu)\Delta\varepsilon_{xx} \quad \Delta\sigma_{yy} = \lambda\Delta\varepsilon_{xx} \quad \Delta\sigma_{zz} = \lambda\Delta\varepsilon_{xx}$$

Figure 6: Essential components of the numerical method to be used for the proposed research

2.2 Model Setup

^{XT:} Add a table for parameters in use. The 3D models has a geometry of $(60\text{km} \times 20\text{km} \times 20\text{km})$ in X, Y and Z axes respectively with a resolution of $\text{dx} = 1\text{km}$ (dx is the length scale for each hexahedron element). For pseudo-2D models, they have a geometry of $(60\text{km} \times 20\text{km} \times 1\text{km})$ in X, Y and Z axes respectively with a resolution of $\text{dx} = 0.5\text{km}$. As shown in Figure 7, temperature linearly increases from 0°C at the top surface to 240°C at the depth of 6 km, reflecting enhanced cooling due to hydrothermal circulation. Below 6 km, the temperature profile follows the semi-infinite half-space cooling model of moving plates [e.g., Turcotte and Schubert, 2002]. Two sides perpendicular to the z coordinate axis are free-slip. The top surface has a vertical traction from water column, of which height is locally determined as $4000 - h(x,z)$ m, where $h(x,z)$ is the topography at a location, (x,z) . The bottom surface is supported by the Winkler foundation. Temperature is fixed at 0°C on the top surface and at 1300°C on the bottom surface. We will adopt the power-law rheology of dry diabase[e.g., Kirby and Kronenberg, 1987, Buck et al., 2005].

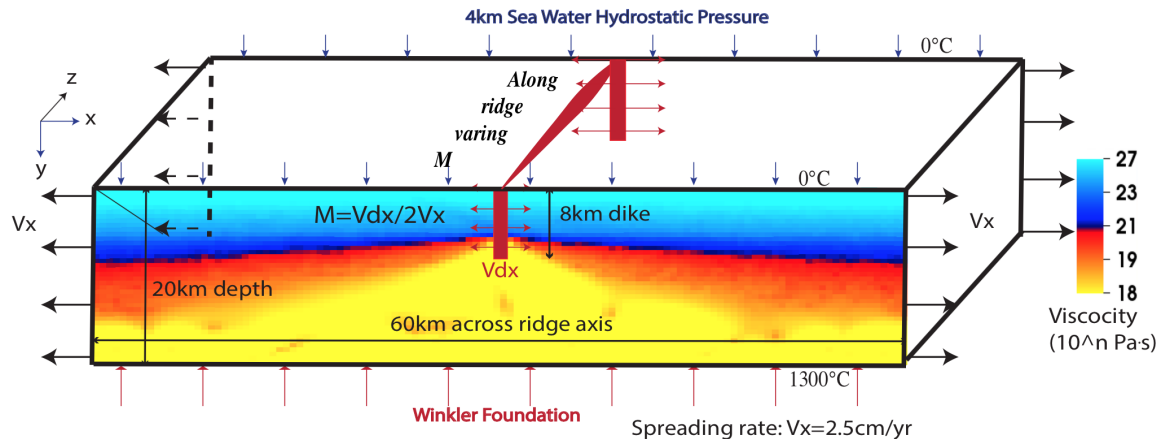


Figure 7: Model setup

2.3 Parameters to control

Although how to estimate the M values from observations has not been well established, we do have constraints from a large dataset of bathymetry, gravity and seismic surveys as

well as geological drilling. Generally, at slow spreading ridges, magma supplies mostly at the center of the ridge segment and decreases towards the end of the segment [Tolstoy et al., 1993, Chen and Lin, 1999]. There is also evidence for shorter wavelength of 10 to 20 km discrete focus of magma accretion along the ridge axis [Lin et al., 1990].

Based on these constraints, we can start considering only a few end-member scenarios of variations in M along the ridge axis. The variation in M is parametrized in terms of the functional forms (e.g. discrete increment, linear, sinusoidal and square root), its wavelength (e.g. 10km, 20km and 40km) and the ranges of M (e.g. 0.2 to 0.8, 0.5 to 0.7 and 0.5 to 0.8).

Preliminary pseudo-2D results show that the model behavior in faulting pattern is sensitive to the rate of strain weakening. Two cases of strain weakening are tested in this study. In one case (denoted as Type 1), cohesion linearly decreases from 44 MPa (denoted as C_i) to 4 MPa (C_e) for plastic strain accumulating from 0 (ε_{p_i}) to 0.1 (ε_{p_e}). It has a characteristic fault slip of 150 meters for pseudo-2D models and 300 meters for 3D models. The other case (Type 2) assumes cohesion linearly decreasing from 44 MPa to 4 MPa for plastic strain accumulating from 0 to 0.33. In this case, the characteristic fault slip for Pseudo-2D models is 500 meters and for 3D models is 1km.

The characteristic fault slip $\Delta X_c = 3 \times dx \times \varepsilon_{p_e}$ (3 is because the thickness of the shear bands is usually 2 to 4 times of the dx [Lavier et al., 2000]) means when ΔX_c amount of displacement takes place at the fault interface, the Cohesion of the material at the faulting interface will decrease to C_e . In this way, under same amount of ΔX_c , models with different resolution should behave in the same way in terms of strain weakening and faulting patterns.

3 3D Results

XT: add one more section as an individual file/chapter for 2D models description. Currently, we have three factors controlling the model behaviors. They are three ranges of M variation along the ridge axis ($0.5\sim0.7$; $0.5\sim0.8$; $0.2\sim0.8$), three functional forms of M variation (linear; sinusoidal; square root) and two types of weakening rate (Type 1 and Type 2) as described in detail in the section “Parameters to control”.

Generally, all models forms a median valley that deepens and widens toward the lower M side except the reference model with constant $M= 0.8$. The topography observed in our models, to the first order, is controlled by the spatial and temporal distributions of faulting and to the second order, results from elastically deformation (e.g. The gradual deepening and widening of the median valley; The bending of the crust at the footwall side of the detachment fault results in a domal shape of the fault interface as a mechanism for producing the dome shape of OCCs).

The pattern of the deformation (faulting and elastic deformation) is controlled by the evolving stress in the crust in terms of its distribution and magnitude. The stress evolution is a result of the interaction processes between tectonics and magmatism. Due to constant seafloor spreading, tensional stress orthogonal to the ridge-axis in the crust keeps accumulating. At the same time, along ridge-axis varying diking partially accommodates the stress from far field extension and perturbs the homogeneity state of stress distribution along the ridge-axis. Accumulated stress will be largely released when the normal or shear failures establish.

In this “Results” chapter, we will first focus on describing model behaviors in detail of two reference models and base on that, we will compare the reference model and the other data points with different setup parameters. Formation mechanism will be explained for part of the the model behaviors in this chapter and will be further discussed in “Discussion” chapter.

3.1 Reference models

We consider two models as our reference models: one, M varies linearly from 0.2 to 0.8 along the ridge axis with increasing Z; two, constant M along the ridge axis as a comparison to the changing M models.

3.1.1 M varies along the ridge-axis

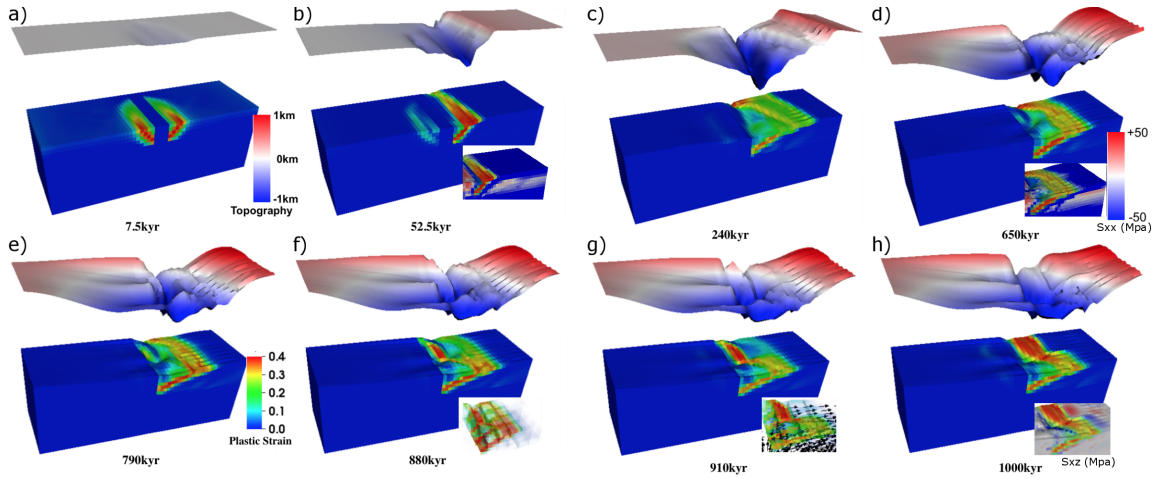


Figure 8: Reference model one: M linearly increases from 0.2 to 0.8 from front to back. The top layer is the topography of the model with five times vertical exaggeration. The color scale within Figure 8.a is for the topography. Initial seafloor is marked as a reference of zero km in height. The green, yellow and red colors in the background of blue model domain are plastic strain. Its color scale is shown in Figure 8.e. The number with kyr as a unit beneath each model result is the time for the model with a unit of thousands of year. The two insets in Figure 8.b and Figure 8.d is for stress σ_{xx} (S_{xx} in the figure). Positive value (pink and red) means tension and negative (blue) is compression. The inset in Figure 8.h is for shear stress σ_{xz} (S_{xz} in the figure). It share the same color scale with insets in the Figure 8.b and Figure 8.d. The inset in Figure 8.f is a transparent view of plastic strain. The inset in Figure 8.g shows both plastic strain and the velocity vector. Indicated by the velocity vector, the hanging wall of the detachment fault at low M region ($M0.2 \sim M0.5$) is moving in an opposite direction to the hanging wall at higher M region ($M > 0.5$).

As shown in Figure 8, the model creates a median valley that both widens and deepens through time and the rate of its widening and deepening at a specific location (in terms of Z-axis) is inverse proportional to the rate of local magma supply (i.e. M value). Kilometers in relief and tens of kilometers in length OCCs are produced in the model. One interesting

behavior worth noting is that corrugations with hundred-to-kilometer wavelengths are also produced by the model.

As shown in Figure 8.a, in the first 7.5kyr, high angle ($\sim 60^\circ$) (consistent with Anderson's theory of faulting mechanics for a frictional angle of 30°) normal faults (shown as higher plastic strain shear bands with a thickness of $2\sim4$ times of the width of a single hexahedron element) begin to form near the ridge axis in terms of plastic strain localization near the ridge center (weakest place to deform), because of the thickness of the crust is thinnest at the ridge center due to our thermal structure setup. For each timestep, the tensional stress accumulates faster at the lower M side where the crust reaches a yielding point earlier than higher M side and so the fault first initiate at the front (lower M side) and then propagates to the back (higher M side). However, the along ridge-axis coupling (internal strength preventing relative displacement (i.e. rotation, offset) between two neighbors along the Z-axis) assists in fault propagation from front to back and reduces the time difference in initiation of faulting along the ridge-axis ^{XT:}when comparing with separate 2D models [It probably will be verified after a 2D results analysis and conclusion].

At 52.5kyr (Figure 8.b), the normal fault on the right hand side of the ridge axis continues to evolve while the one on the left becomes inactive. The choice of which fault will develop is a random event since the model setup is symmetrical across the ridge-axis. The timing difference of initiation of faulting along the ridge axis creates an offset in X-axis direction between along ridge-axis breakways that the breakaway at the lower M side extends further than that of the higher M side (Figure 10). This offset remains constantly around three elements until time 295kyr (Figure 10.d) because the extending velocity of the breakaway to move away from the ridge-axis is only controlled by the far field extension rate, V_x . ^{XT:}Why after 295kyr the offset reduces needs to be answered. I don't know now. Probably partly due to healing that earlier the fault initiation, more healing it experiences. In addition, as shown in the inset of σ_{xx} , as the fault offsets, crust at the footwall begins to bend in a clockwise rotation (view from front) and the neutral plane ($\sigma_{xx} = 0$) is shown as

the boundary between blue (compression) and pink (tension). In the “Discussion” section, we will show that this bending force created in the crust of footwall is essential for major faulting evolution.

The location of the termination of the detachment fault where footwall begins to be exhumed to the surface varies along the ridge-axis (i.e. Z-axis). As shown in Figure 9, the highest strain rate regions (red) can be interpreted as detachment fault interfaces. When $M \leq 0.5$, although the rate of fault slip should be higher for lower M, the rate of bending or decreasing in dip angle of the fault has a maximum value corresponds to the far field extension rate. Because for $M < 0.5$, the detachments root at the same place (center dike at a depth five to six elements beneath the surface)(Figure 9.Z=0, 5, 10) along the ridge-axis, the amount of bending in the footwall of the detachment is determined by the amount of the displacement of the breakaway. In other words, because in order to spend least frictional energy during faulting, fault interface between the two ends tends to be a straight line. Thus, the dip angle of the fault is inverse proportional to the distance between the breakaway and the root of the normal fault when $M < 0.5$. So the further between the breakaway and the root of the fault, the lower its dip angle. Since the breakaways at the region with $M < 0.5$ is pulled with the same velocity V_x , the distances between the breakaways and the roots of the faults are the same. Thus the dip angles of the faults at the same time along the ridge-axis are the same. However, when $M > 0.5$, the amount of fault slip decreases as M increase and the crust at the footwall experiences less bending and the detachment remains in high angle with closer to ridge-axis termination (Figure 9.Z=15, 20). This is due to the root of the fault is being slowly pushed away from ridge-axis while the breakaway of the fault is closer to ridge center since the fault initiates later than that at the low M side. In addition, the crust thickness the fault cut through is slowly increasing as the fault being pushed away from ridge center due to excessive diking. These three factors together contribute to a higher dip angle. In a unit time, the volume of the exhumation is also smaller for the higher M side. One thing needs to be noted that the lowest topography points at high M side correspond to

the terminations but detached from the terminations at the low M side ($M < 0.5$) as shown in Figure 9.

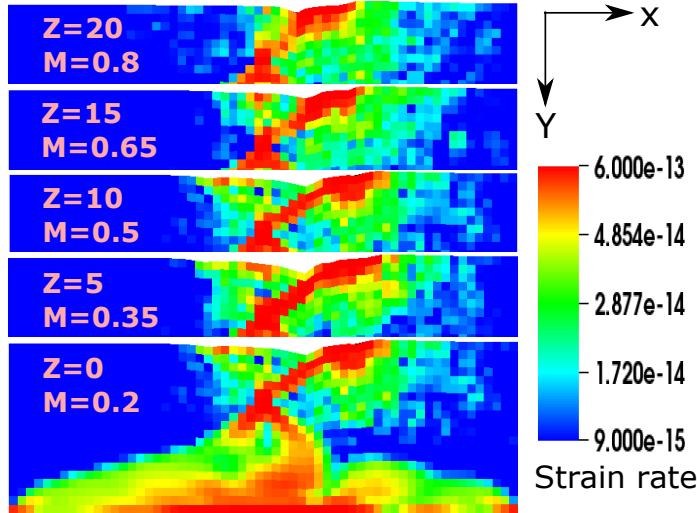


Figure 9: Strain rate at 107.5kyr with five slices along ridge axis(Z axis).

At 240kyr (Figure 8.c), the median valley further deepens and widens. The detachment keeps active and extends to $\sim 18\text{km}$ in length horizontally (longest at $M = 0.2$) with the dip angle decreases from initially $\sim 60^\circ$ to 30° (at the root of the fault) and 0° where the fault interface is exposed to the seafloor. However, for the detachment at the higher M side (especially the last three elements along the Z-axis), the dip angle remains high. The maximum relief between highest point in breakaway and lowest point in the median valley becomes larger than 1km. Corrugations show up at the lower M side, at the front tip of the extending fault interface. The lowest topography points inside the median valley evolves from a straight line parallel to the ridge-axis (Figure 10.a) to a line oblique to the ridge-axis (Figure 10.b,c,d). Initially, the lowest topography points are at the terminations of the detachment fault. Due to the coupling along the ridge-axis, fault propagates from front to back in a straight line parallel to the ridge-axis. However, as the dip angle of the detachment at the low M side begin to decrease due to bending of the crust at the footwall, along with excessive tensional stress result from low magma supply, the lowest topography point at the lower M side is pulled to the conjugate plate. While the lowest topography points at

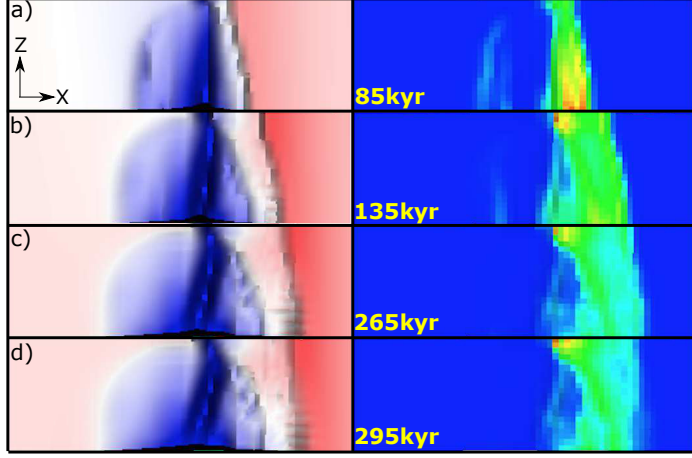


Figure 10: Breakaway evolution through time. Viewing from top. Left column is topography at different time; Right column is plastic strain. They both share same color scales in the figure 8. The offset between breakways along the ridge-axis in X-axis direction remains three elements until time 295kyr. It also shows that the lowest topography points along the ridge-axis start as a straight line parallel with ridge-axis in a) and then gradually become oblique to the ridge-axis. Please see text for detail description.

the high M side ($M > 0.5$) are pushed away from the dike. Note that the oblique lowest topography points form not a straight line, but a curve that the lowest point remains near axis at the high M side. This is due to the bending rate of the detachment at high M side is very low and thus the termination can remains near the ridge-axis.

XT: One question needs to be answered: at 410 timesteps (205kyr), the breakaway at the front already extends 15km, assuming a constant extending rate, it means a velocity of around 75km/Myr, much faster than half spreading rate 25km/Myr. If it is true, I need to change previous discussion on how fast breakaway being pulled away from ridge-axis.

At 650kyr (Figure 8.d), the median valley continues to deepen and widen. The breakaways along the ridge-axis already *XT:* moved out of the model domain [it should not, if breakaway move with 25km/yr(half spreading rate), since the distance between initial break (5km away from ridge center) and right wall of the model domain is about 25km which needs 1Myr to reach. But now is only 650kyr. Why is it?]. The fault offset is already larger than the thickness of the crust and the upper mantle materials begin to be exhumed to the surface. The previous fault interface bend over to a negative dip angle (dip in an

opposite direction) and produces a dome shape OCC with corrugations on its surface parallel to the spreading direction. The previous lowest topography points evolve to a curve with bigger curvature. Compared to the inset in Figure 8.b, the total length of the bending crust decreases. A hint of a near-axis secondary fault begin to initial at the high M side ($10 < Z < 15$) as a form of tension failure. ^{XT:}Its formation will be discussed in Discussion section accompanied by the stress status analysis.

At 790kyr (Figure 8.e), the initial tension failure immediately adjacent to the ridge center (hint of the secondary fault) begin to evolve and propagate to higher Z region.

At 880kyr (Figure 8.f), at the higher M side, the initial tension failure evolves to a high angle near-axis secondary normal fault and replace the initial detachment as indicated in the inset of transparent view of plastic strain.

At 910kyr (Figure 8.g), the secondary normal fault results in a strong contrast in moving directions between high M side and low M side near the ridge-axis that at the high M side, previous hanging wall becomes footwall and moves with spreading direction on the right, however, at the low M side, due to deficit in magma supply, hanging wall is coupled with conjugate plate and move to the left as shown in the inset. This opposite direction motion creates a strong shear stress region $\sim 45^\circ$ oblique to the ridge-axis (inset of Figure 8.h) and produces new lowest topography points align with it. Combined with previous lowest topography points, an “X” shape topography low is created.

Corrugations are observed in the model since 240kyr. It will be further discussed in the discussion chapter. There are two contributing factors, for one, trans-extenstional stresses are created due to offset of the breakaway as well as the variation in fault displacements along the ridge axis; for the other, the variation of the positions of the terminations of the detachment faults along the ridge-axis creates anastomosing faults that is mentioned in [Smith et al., 2014]. This anastomosing faulting behavior is largely responsible for corrugations in our models.

3.1.2 Constant M along the ridge-axis

Another reference model is the model with constant $M= 0.8$ along the ridge axis as a comparison to the changing M models.

As shown in Figure 11, this constant M along the ridge-axis model create a median valley of $\sim 20\text{km}$ in width and $1 \sim 2\text{km}$ in depth which is similar to generally observation of Mid-Atlantic Ridges. The width and depth of the median valley is almost constant along the ridge-axis. The variation along the ridge-axis in breakaway and termination as well as the existence of corrugation mentioned in reference model one are not observed.

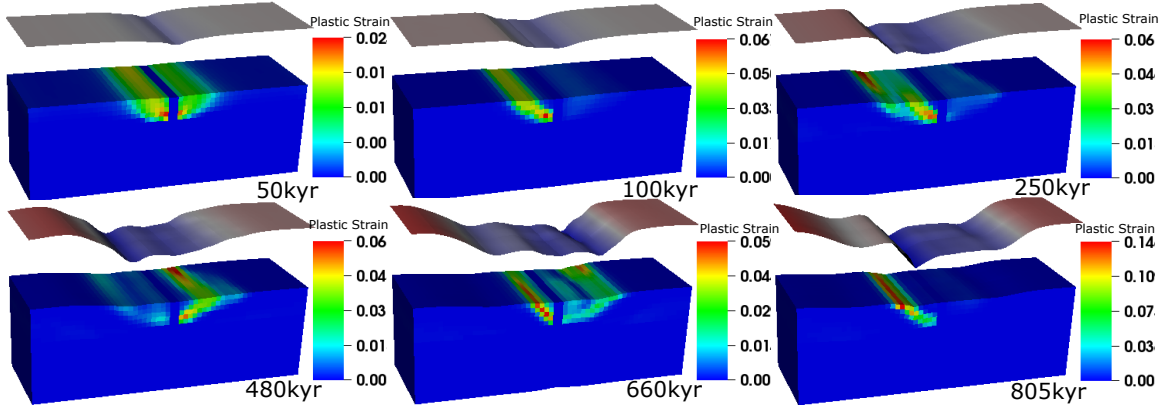


Figure 11: Reference model two: constant $M= 0.8$ along the ridge-axis (i.e. Z axis). Type two weakening.

Based on the previous experience in pseudo-2D models or [Lavier et al., 2000], with higher characteristic fault offset (ΔX_c) for Type two weakening compared with Type one weakening, the frequency of normal faulting alternation is higher for $M > 0.5$ cases. However, interesting enough, when comparing pseudo-2D and 3D models when they are using Type two weakening under case of $M= 0.8$, even though the 3D Model has a larger ΔX_c of 1km than that of pseudo-2D model of 0.5km, 3D model has a lower frequency of faulting alternation. Since M is constant 0.8 along the ridge-axis, the effect of along ridge coupling that resists alternation need not be considered. One possibility is that the resisting bending force increase in a higher rate than linear with respect to increasing the length of the ridge segment (Z_{max} km).

3.2 Tables of all the data points

Currently, we have run ~~XT:hundreds of~~ [find out exactly number that will be used in 2D model results conclusion] Pseudo-2D models for initial setup and benchmarking with previous studies (e.g. [Buck et al., 2005] and [Tucholke et al., 2008]). Based on those Pseudo-2D models, we further ran 11 3D models. The available data points are limited due to the huge computation expenses for 3D models (For each model to be run to 2Myr, usually needs 192 cores for about 2 days (around 10000 SUs). ~~XT:use 96 cores can improve the efficiency a little bit (Longer time but smaller amount of SUs needed).~~

A	Alternating Fault	C	Corrugation	SL	Shear Topography Low
NA	Not Alternating	SF	Secondary Fault on one side	CB	Cut Back
DD	Double Dome	AM	Atlantis Massif		

Table 1: Model behaviors in short.

Based on the 11 models, we observed eight first-order behaviors as shown in Table 1.

M range Weakening type	M28	M57	M58
Type one	NA; C; SL; SF _{1500kyr} ; DD	NA; C; SF _{1380kyr} ; CB _{330kyr} ; AM(opposite z)	
Type two			

Table 2: Linear functional form.

M range Weakening type	M28	M57	M58
Type one	NA; C; SL; SF _{995kyr}	NA; C; SL; SF _{760kyr;1320kyr} ; CB _{520kyr} ; AM	NA; C; SL; CB _{510kyr} ; SF _{760kyr;1140kyr;1990kyr}
Type two		NA; C; SL; SF _{680kyr} ; CB _{905kyr}	A _{450kyr;600kyr} ; C(only at low M); CB _{990kyr}

Table 3: Sinusoidal functional form.

M range Weakening type	M28	M57	M58
Type one	NA; C; SL; CB _{205kyr;330kyr;1025kyr}		NA; C _{1770kyr} (due to shear with dif wave length); SF _{860kyr} (high M); SF _{1190kyr} (low M)(Dog Bone); SF _{1690kyr}
Type two		NA; C; SF _{435kyr;1060kyr} ; CB _{585kyr} ; CB _{735kyr} ; CB _{910kyr} ; CB _{970kyr}	A _{550kyr;920kyr} ; C; CB _{400kyr}

Table 4: Square root functional form.

Based on the available data points as shown in the tables, we are able to compare the model results with respect to three factors: 1) Variation of the range of M; 2) Variation of the functional form and 3) Influence of weakening rate.

3.3 Variation of the functional form

How magma supply varies along the MORs ridge-axis remains a current research question and we do not have direct quantitative observation over it. However, from indirect geo-physical studies (e.g. gravity, seismology), people suggest a general qualitative pattern of 20 to 50 km long second-order ridge segment with magma mostly supply at the segment center and decreases to the end. Since we do not know exactly how magma supply varies along the ridge, we try three functional forms (linear, sinusoidal and square root) for its variation along the ridge-axis. According to our model results, different functional forms with same M range are generally similar with minor differences.

3.3.1 Comparing M28 in terms of linear, sinusoidal and square root

As shown in the tables, M28 with Type one weakening is the only M range that has three functional forms data points available. Initially, due to There are two phenomena that show distinct differences with respect to different functional forms. One is the geometry and timing of the secondary fault. The other is the “Cut back” behavior mostly observed in the square root model.

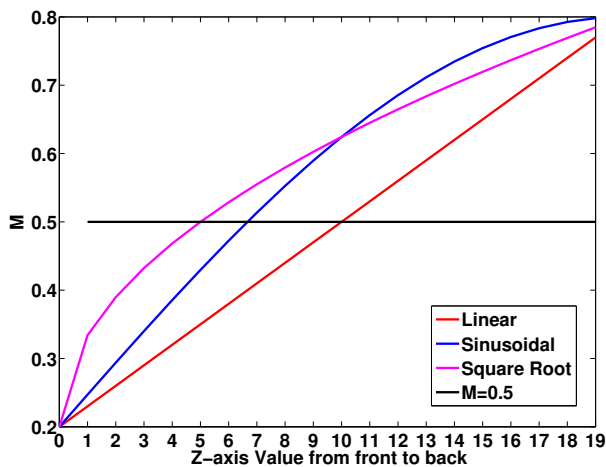


Figure 12: Three functional forms of M variation comparison. They begin to exceed the $M = 0.5$ black line at $Z = 10, 7, 5$ for linear, sinusoidal and square root respectively.

Secondary Fault For linear, the secondary fault at higher M side begins to take place at around 900kyrs (Figure 13), its spatial distribution is at $M > 0.5$ region. It nucleates from the shear low (ridge center where $M = 0.5$) to the $M = 0.8$ end (Figure 12 where the red line begin to exceeds 0.5 at $Z = 10$). As it evolve, the initial detachment becomes inactive. This secondary fault creates another dome with initial composition likely to be volcanic rather than ultramafic, however, as it evolves, if it can last long enough to cut through the whole crust, mantle materials might exhumed to the surface. The composition of the domes observed at Kane magamullions is similar to this mechanism between ultramafic babel dome and eastern to it the crustal inside-corner high.

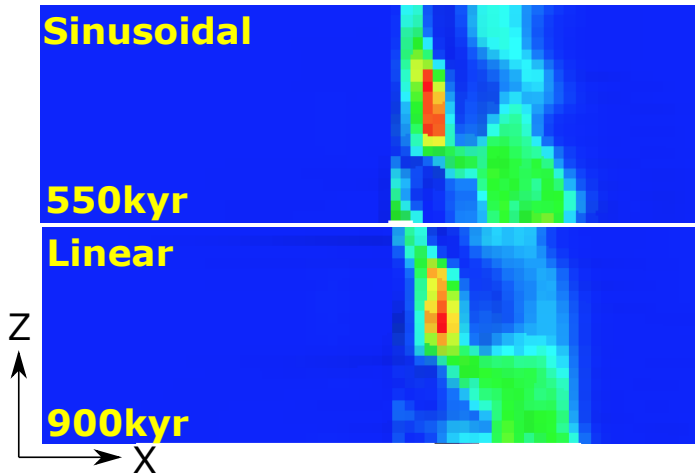


Figure 13: Secondary fault length comparison between linear and sinusoidal. Around 13 elements in length for sinusoidal compared to 11 elements for linear.

For sinusoidal, the secondary fault begins to form at a much earlier time around 550kyrs (Figure 13), this is due to the total area above $M > 0.5$ for sinusoidal functional form is higher than that of linear. Qualitatively, the total force to push the hanging wall of the detachment away from the dike for sinusoidal is larger than that of linear. The larger the force, the faster the detachment move off axis, the earlier the secondary fault will appear. In addition, the total length of the secondary fault is longer due to the total length of M that is above 0.5 is bigger than that of the linear model (Figure 12). For square root, there is no secondary fault forming because the “cut back” behavior releases the tensional stress in the

hanging wall.

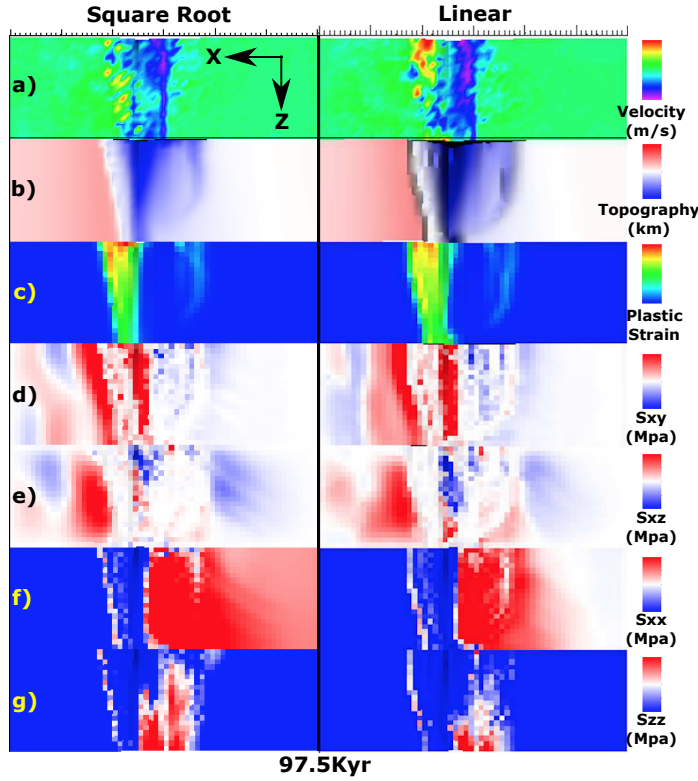


Figure 14: View from top of the model.

Cut back The cut back happens mostly in the square root model. Since the linear model and the square root model have more obvious difference in terms of the cut back behavior, here, we only compare linear and square root. There are several factors contribute to the cut back behavior. First, at the higher M side, the amount of diking for the square root model is ubiquitously larger than that of the linear one (Figure 12). This leads to a slower bending detachment at the high M side for the square root model. Second, the total length of the ridge segment with $M > 0.5$ for the square root model is also longer than that of the linear one (Figure 12). This results in that at the low M side, σ_{xz} is focused at low Z adjacent to the ridge-axis (Figure 14.e), however for linear is spread out to Z higher than 10. Third, due to higher value of $\frac{dM}{dZ}$ for square root when $Z < 5$, the along ridge-axis shear σ_{xz} for square root will be accumulating faster, which produces larger strike-slip force to

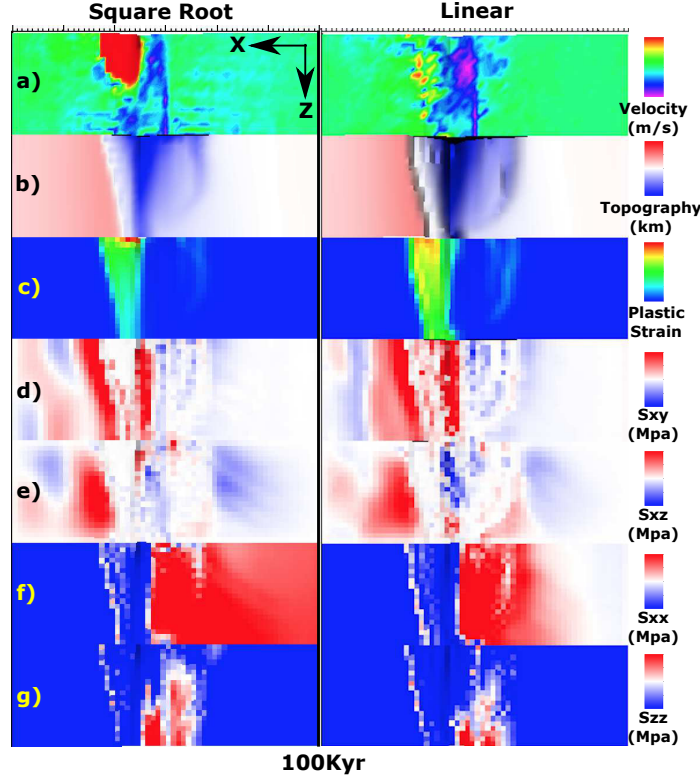


Figure 15: View from top of the model.

cut the hanging wall at the low M side. Fourth, as observed in the model (Figure 14.c), the parallel to spreading direction offset between breakaways along the ridge-axis is 4km for the square root model compared to 3km for the linear model. This causes the square root model to experience bigger shear stress σ_{xy} both immediately beneath and above the fault interface at the low M side (Figure 14.d). All together lead to the decouple of the hanging wall at the low M side.

(^{XT}:this fault scarp behavior will be shown much obvious in the topography with different viewing angle (to be added) and even better at time 160kyr(must be added)).

As shown in Figure 16, at the tip of the breakaway at the low M side. the hanging wall rebounds backwards to the dike in a high velocity with a suddenly topography drop (Figure 16.b,c(second row)).

3.4 Variation of the range of M

We have three ranges for M variation along the ridge-axis: M28, M57 and M58 (M28 means M varies from 0.2 to 0.8 from front to end as Z increases). One distinct difference between M58 and M57 or M28 is only models with range M58 produce fault alternation.

3.5 Influence of weakening rate

[Lavier et al., 2000] shows higher characteristic fault offset result in more multiple fault. Only Type two weakening can produce alternating normal fault.

3.6 Fault Alternation

The fault alternation behavior observed in pseudo-2D models in cases $M > 0.5$ is much more complicated in 3D models. The results shows that only Type two weakening with M58 will result in a alternating faulting pattern. ^{XT:}integrate the area of $M > 0.5$ with respect to Z to see if there is any quantatative analysis available.

3.7 Corrugation

The stress at the tips of the breakaways is generally tensional in both parallel and orthogonal directions to the ridge-axis. (Figure 14.f,g)

3.8 Summary of Findings

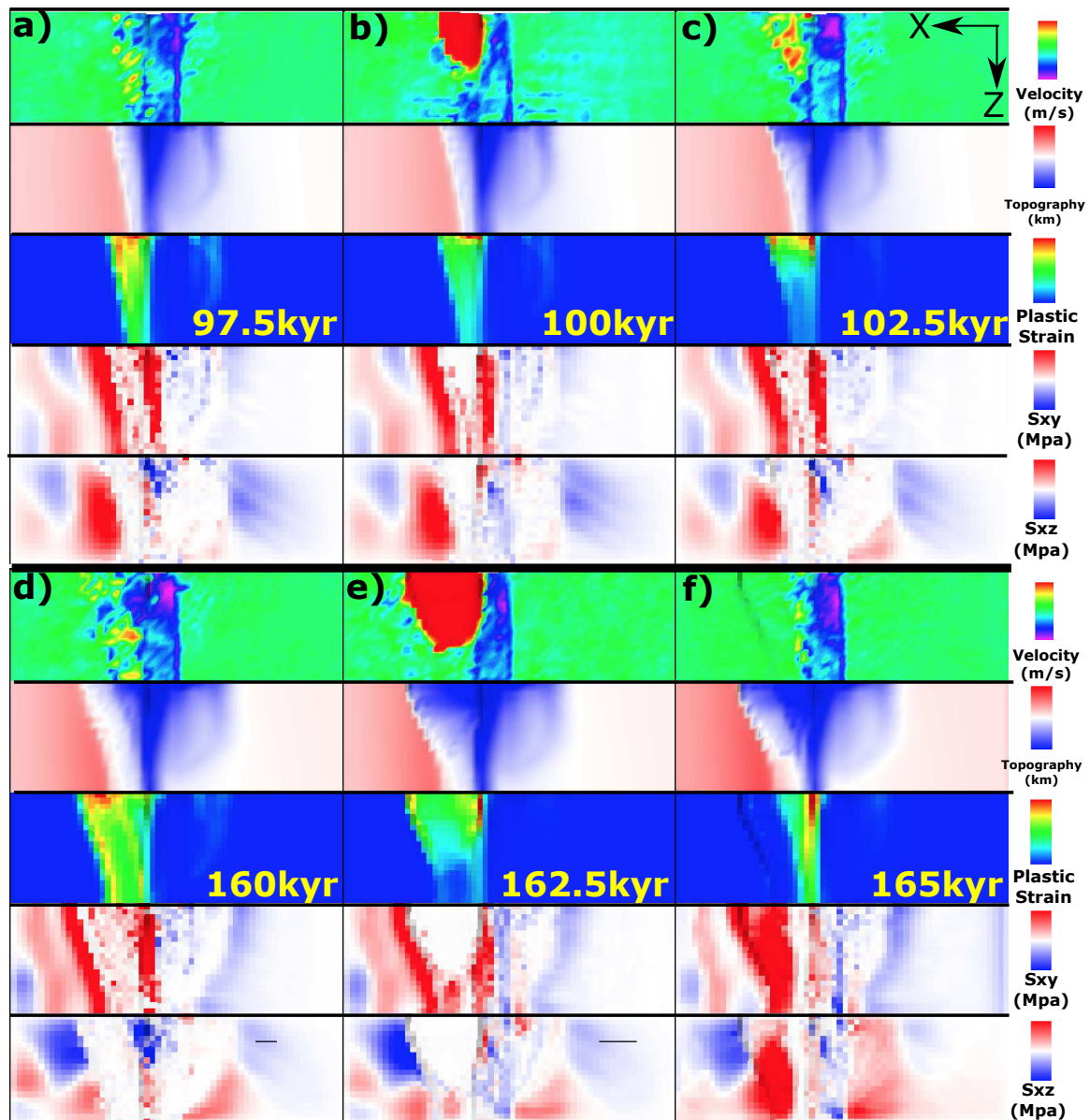


Figure 16: Cut back behaviors in square root functional form model with different time.

4 Discussion

Since the model behavior is very complicated. We will focus on the effects being brought by the along ridge-axis variation in diking. Thus, it is worth considering a thought experiment with two end members: One, the along ridge-axis coupling is rigid, so that even along ridge axis variation in M exist, once a fault determined to develop, it will cut through the whole model domain along the ridge-axis(Z-axis) simultaneously. The other end member is that there is totally no coupling along the ridge-axis. So that each slice of crossection profile across the ridge behave separately without being influenced by its neighbour to a extreme that the model behavior is just a combination of 20 pseudo-2D models piled up along ridge-axis with their own M . (IMPORTANT: this suggests the importance and urgence for making clear conclusion and results description for previous pseudo-2D models results. However, one difficulty here is that the characteristic fault offset ΔX_c is different between 2D and 3D models.)

4.1 Discussion of Findings

4.2 Fault alternation

4.2.1 Alternating on conjugate plate

4.2.2 Secondary near-axis normal fault

The secondary near axis high angle normal fault is another common observation of the models. As shown in Figure 8, at the ridge axis with $M > 0.5$ (i.e. $Z > 10$), the existing normal fault will be pushed away from the ridge-axis due to excessive diking, as its mechanism has been mentioned in the introduction chapter, another new near axis normal fault is created at around 650kyr. As it evolve, the initial detachment fault become inactive (the transparent view of plastic strain shown in the rigth corner inset of time 880kyr). This secondary fault creates another dome and its composition is more likely to be volcanic rather

than ultramafic, however, as it evolves, if it can last long, lower crust and upper mantle material can be exhumed to the surface. The composition of the domes observed at Kane magamullions is similar to this mechanism that ultramafic Babel dome is on the West and crustal inside-corner high on the East.

4.3 Influence of healing

4.4 Comparing model results with nature observation

4.5 Parallel computing efficiency

4.6 Model Limitation

4.7 Recommendation for Future Research

5 Conclusions

References

- G. Baines, M. J. Cheadle, B. E. John, and J. J. Schwartz. The rate of oceanic detachment faulting at atlantis bank, sw indian ridge. *Earth and Planetary Science Letters*, 273(1-2):105–114, Aug. 2008. ISSN 0012821X. doi: 10.1016/j.epsl.2008.06.013.
- R. Buck, L. Lavier, and A. Poliakov. Modes of faulting at mid-ocean ridges. *Nature*, 434(7034):719–23, 2005. ISSN 1476-4687. doi: 10.1038/nature03358.
- Y. J. Chen and J. Lin. Mechanisms for the formation of ridge-axis topography at slow-spreading ridges: A lithospheric-plate flexural model. *Geophysical Journal International*, 136:8–18, 1999. ISSN 0956540X. doi: 10.1046/j.1365-246X.1999.00716.x.
- E. Choi, L. Lavier, and M. Gurnis. Thermomechanics of mid-ocean ridge segmentation. *Physics of the Earth and Planetary Interiors*, 171(1-4):374–386, Dec. 2008. ISSN 00319201. doi: 10.1016/j.pepi.2008.08.010.
- C. M. R. Fowler. *The solid earth: an introduction to global geophysics*. Cambridge University Press, 2004.
- S. Kirby and A. K. Kronenberg. Rheology of the lithosphere: Selected topics. *Reviews of Geophysics*, 25(6):1219–1244, 1987.
- L. L. Lavier, W. R. Buck, and A. N. B. Poliakov. Factors controlling normal fault offset in an ideal brittle layer. *Journal of Geophysical Research*, 105(B10):23431, 2000. doi: 10.1029/2000JB900108.
- J. Lin, G. M. Purdy, H. Schouten, J.-C. Sempere, and C. Zervas. Evidence from gravity data for focused magmatic accretion along the Mid-Atlantic Ridge. *Nature*, 344:627–632, 1990. ISSN 0028-0836. doi: 10.1038/344627a0.
- W. B. F. Ryan, S. M. Carbotte, J. O. Coplan, S. O’Hara, A. Melkonian, R. Arko, R. A. Weisel, V. Ferrini, A. Goodwillie, F. Nitsche, J. Bonczkowski, and R. Zemsky. Global multi-

resolution topography synthesis. *Geochemistry, Geophysics, Geosystems*, 10, 2009.
ISSN 15252027. doi: 10.1029/2008GC002332.

D. K. Smith, H. Schouten, H. J. B. Dick, J. R. Cann, V. Salters, H. R. Marschall, F. Ji, D. Yoerger, A. Sanfilippo, R. Parnell-turner, C. Palmiotto, A. Zhelezov, H. Bai, W. Junkin, B. Urann, S. Dick, M. Sulanowska, P. Lemmond, and S. Curry. Development and evolution of detachment faulting along 50 km of the mid-atlantic ridge near 16.5°n. *Geochemistry Geophysics Geosystems*, pages 4692–4711, 2014. doi: 10.1002/2014GC005563.Received.

M. Tolstoy, A. J. Harding, and J. A. Orcutt. Crustal Thickness on the Mid-Atlantic Ridge: Bull's-Eye Gravity Anomalies and Focused Accretion. *Science*, 262(October):726–729, 1993. ISSN 0036-8075. doi: 10.1126/science.262.5134.726.

B. E. Tucholke, M. D. Behn, W. R. Buck, and J. Lin. Role of melt supply in oceanic detachment faulting and formation of megamullions. *Geology*, 36(6):455, 2008. ISSN 0091-7613. doi: 10.1130/G24639A.1.

D. L. Turcotte and G. Schubert. *Geodynamics*. Cambridge, 2002.